AIAA JOURNAL
Vol. 40, No. 10, October 2002

Numerical Method for Vorticity Confinement in Compressible Flow

Guangchu Hu* and Bernard Grossman†
Virginia Polytechnic Institute and State University, Blacksburg, Virginia 24061
and
John Steinhoff‡
University of Tennessee Space Institute, Tullahoma, Tennessee 37388

It is well known that modern computational fluid dynamics codes based on Eulerian descriptions do not adequately handle flows involving the convection of thin vortical layers. These layers often remain very thin and persist long distances without significant dissipation. Over the past decade, Steinhoff has introduced a class of methods, generally known as "vorticity confinement," which have been used successfully to predict complex flows, particularly involving helicopter rotors. These methods have involved an incompressible finite difference formulation. We extend vorticity confinement to compressible flows by noting that the confinement term added to the momentum equation in Steinhoff's formulation may be interpreted as a body force. We can then extend the approach to compressible flows by adding the contribution of this body force to the integral conservation laws. The development of a finite volume compressible vorticity confinement scheme then follows directly. We have implemented the scheme with a matrix artificial dissipation and a new matrix confinement term. Results are presented for supersonic shear layers, vortices moving in a uniform stream, and vortex separation on the leeward surface of a flat plate delta wing at supersonic speed.

Nomenclature

$\boldsymbol{A}, \boldsymbol{B}$	=	flux Jacobians $\partial \boldsymbol{F}/\partial \boldsymbol{Q}$, $\partial \boldsymbol{G}/\partial \boldsymbol{Q}$
a	=	local speed of sound
b	=	half-span of a delta wing
C_p	=	pressure coefficient
$D^{(2)}, D^{(4)}$	=	second- and fourth-order dissipation terms for matrix dissipation model (MDM[(1)])
e_0	=	total energy per unit mass
$\boldsymbol{F}, \boldsymbol{G}$	=	Cartesian components of the inviscid flux vector
$\boldsymbol{f}_b$	=	vector body force per unit mass
h_0	=	stagnation enthalpy per unit mass
$\hat{i}, \hat{j}, \hat{k}$	=	unit vectors in Cartesian coordinates x, y, z, respectively
k	=	grid stretching parameter; Eq. (28)
$\boldsymbol{k}$	=	vorticity confinement vector in incompressible flows; Eq. (3)
$\hat{n}$	=	unit vector in the direction opposite to the gradient of the vorticity magnitude; Eqs. (4) and (35)
p	=	pressure
$\boldsymbol{Q}$	=	vector of conservative variables
R_c, R_o	=	vortex core radius and vortex radius for initial conditions in isolated vortex calculation; Eqs. (26) and (27)
$\boldsymbol{R}(\boldsymbol{Q})$	=	residual vector
r, ξ, η	=	conical coordinates; Eq. (29)
$\boldsymbol{S}$	=	vorticity confinement vector
$\boldsymbol{T}$	=	matrix whose columns are composed of the eigenvectors of A
U_c, U_o	=	vortex core velocity and vortex outer velocity for initial conditions in isolated vortex calculation; Eqs. (26) and (27)
u, v, w	=	Cartesian velocity components
x, y, z	=	Cartesian coordinates
β	=	grid stretching parameter; Eq. (28)
γ	=	pressure filter parameter in MDM[(1)]
$\Delta \mathcal{S}_k$	=	surface area of cell side k; Eq. (15)
$\Delta \mathcal{V}_{i,j}$	=	volume of cell i, j; Eq. (15)
Δx	=	axial grid spacing
ϵ_c, ϵ_c'	=	confinement parameter for scalar and matrix confinement, respectively
ϵ_d	=	dissipation parameter for MDM[(2)]
ϵ_2, ϵ_4	=	second- and fourth-order dissipation parameters for MDM[(1)]
Λ	=	diagonal matrix whose elements are the eigenvalues of $\boldsymbol{A}$
ν	=	kinematic viscosity
ρ	=	density
$\boldsymbol{\omega}$	=	vorticity vector

Subscript

∞	=	freestream

Received 29 January 2001; revision received 7 May 2002; accepted for publication 7 May 2002.

*Graduate Research Assistant, Department of Aerospace and Ocean Engineering; currently Research Associate, Department of Mechanical Engineering. Member AIAA.

†Professor and Department Head, Department of Aerospace and Ocean Engineering. Fellow AIAA.

‡Professor, Department of Engineering Science and Mechanics.

Introduction

THE original formulation of the vorticity confinement method of Steinhoff et al.[1] and Steinhoff[2] began with an additional confinement term added to the incompressible Navier–Stokes equations as follows:

$$\nabla \cdot \boldsymbol{V} = 0 \tag{1}$$

$$\partial_t \boldsymbol{V} = -(\boldsymbol{V} \cdot \nabla)\boldsymbol{V} - \nabla(p/\rho) + \nu \nabla^2 \boldsymbol{V} + \epsilon \boldsymbol{k} \tag{2}$$

where the confinement term was written in terms of a constant ϵ and a vector $\boldsymbol{k}$ defined in terms of the vorticity $\boldsymbol{\omega} \equiv \nabla \times \boldsymbol{V}$ as

$$\boldsymbol{k} = -\hat{\boldsymbol{n}} \times \boldsymbol{\omega} \tag{3}$$

with the vector $\hat{\boldsymbol{n}}$ in the direction opposite to the gradient of the vorticity magnitude as

$$\hat{\boldsymbol{n}} = \frac{-\nabla(|\boldsymbol{\omega}|)}{|\nabla(|\boldsymbol{\omega}|)|} \tag{4}$$

The confinement term has been designed to transport back vorticity, which has been diffused by the numerical scheme. The confinement adds an acceleration in a direction that is normal to the vorticity and to the gradient of vorticity. This has the effect of adding a velocity correction that convects $\boldsymbol{\omega}$ in the opposite direction of the numerical diffusion. For further discussion, see Ref. 2. An alternate explanation of the workings of vorticity confinement in terms of solitary waves appears in Refs. 3 and 4.

Compressible Formulation

There have been several attempts to extend the vorticity confinement to compressible flows. The central issue was how to add the confinement term in a consistent manner within a conservation law framework. Pevchin et al.[5] developed a complicated formulation based on flux splitting that was dependant on the grid orientation. Yee and Lee[6] attempted to utilize the incompressible confinement term into the compressible momentum equations.

The present approach represents somewhat of a breakthrough in solving the problem. We have noticed that the confinement may be considered to be a body force that may be added to the integral momentum equation and the rate of work done by the body force added to the energy conservation law. The integral conservation laws for mass, momentum, and energy may be written for a control volume fixed in space as

$$\frac{\mathrm{d}}{\mathrm{d}t}\iiint_{\mathcal{V}} \rho \,\mathrm{d}\tau + \iint_{\mathcal{S}} \rho \boldsymbol{V}\cdot\hat{\boldsymbol{n}}\,\mathrm{d}\sigma = 0 \tag{5}$$

$$\frac{\mathrm{d}}{\mathrm{d}t}\iiint_{\mathcal{V}} \rho \boldsymbol{V}\,\mathrm{d}\tau + \iint_{\mathcal{S}} \rho \boldsymbol{V}(\boldsymbol{V}\cdot\hat{\boldsymbol{n}})\,\mathrm{d}\sigma = -\iint_{\mathcal{S}} p\hat{\boldsymbol{n}}\,\mathrm{d}\sigma + \iiint_{\mathcal{V}} \rho \boldsymbol{f}_b\,\mathrm{d}\tau \tag{6}$$

$$\frac{\mathrm{d}}{\mathrm{d}t}\iiint_{\mathcal{V}} \rho e_0\,\mathrm{d}\tau + \iint_{\mathcal{S}} \rho e_0 \boldsymbol{V}\cdot\hat{\boldsymbol{n}}\,\mathrm{d}\sigma = -\iint_{\mathcal{S}} p\boldsymbol{V}\cdot\hat{\boldsymbol{n}}\,\mathrm{d}\sigma + \iiint_{\mathcal{V}} \rho \boldsymbol{V}\cdot\boldsymbol{f}_b\,\mathrm{d}\tau \tag{7}$$

where $\boldsymbol{f}_b$ is a body force per unit mass (acceleration). We have presented the inviscid, adiabatic form of the equations here, but the extension to viscous flows is straightforward.

Now, to develop a compressible confinement formulation, we take this body force term to be defined as

$$\boldsymbol{f}_b = -\epsilon_c \hat{\boldsymbol{n}} \times \boldsymbol{\omega} \tag{8}$$

where $\hat{\boldsymbol{n}}$ is defined in Eq. (4) and ϵ_c is a confinement parameter. Equations (5–8) may be used directly to develop a finite volume discretization. It is often helpful to consider the resulting differential equations, which may be developed directly after an application of Gauss's theorem. For two-dimensional inviscid flow in Cartesian coordinates, we obtain

$$\frac{\partial \boldsymbol{Q}}{\partial t} + \frac{\partial \boldsymbol{F}}{\partial x} + \frac{\partial \boldsymbol{G}}{\partial y} = -\boldsymbol{S} \tag{9}$$

where

$$\boldsymbol{Q} = \begin{pmatrix} \rho \\ \rho u \\ \rho v \\ \rho e_0 \end{pmatrix}, \qquad \boldsymbol{F} = \begin{pmatrix} \rho u \\ \rho u^2 + p \\ \rho uv \\ \rho u h_0 \end{pmatrix}, \qquad \boldsymbol{G} = \begin{pmatrix} \rho v \\ \rho uv \\ \rho v^2 + p \\ \rho v h_0 \end{pmatrix} \tag{10}$$

$$\boldsymbol{S} = \begin{pmatrix} 0 \\ \epsilon_c \rho(\hat{n}\times\boldsymbol{\omega})\cdot\hat{i} \\ \epsilon_c \rho(\hat{n}\times\boldsymbol{\omega})\cdot\hat{j} \\ \epsilon_c \rho(\hat{n}\times\boldsymbol{\omega})\cdot\boldsymbol{V} \end{pmatrix} = \begin{pmatrix} 0 \\ \epsilon_c \rho n_y \omega_z \\ -\epsilon_c \rho n_x \omega_z \\ \epsilon_c \rho(u n_y - v n_x)\omega_z \end{pmatrix} \tag{11}$$

The vector $\hat{\boldsymbol{n}}$ is

$$\hat{\boldsymbol{n}} = -\frac{\nabla(|\omega_z|)}{|\nabla(|\omega_z|)|} \tag{12}$$

with

$$\omega_z = \frac{\partial v}{\partial x} - \frac{\partial u}{\partial y} \tag{13}$$

Numerical Formulation

We discretize Eq. (9) using a finite volume method. We utilize an explicit time integration with a four-stage Runge–Kutta time stepping scheme as

$$\boldsymbol{Q}^{(l)} = \boldsymbol{Q}^{(0)} + \alpha_l \Delta t \boldsymbol{R}\big(\boldsymbol{Q}^{(l-1)}\big) \tag{14}$$

for $l = 1, \ldots, 4$ and $\alpha_1 = \frac{1}{4}$, $\alpha_2 = \frac{1}{3}$, $\alpha_3 = \frac{1}{2}$, and $\alpha_4 = 1$, with the residual defined as

$$\boldsymbol{R}\big(\boldsymbol{Q}^{(l-1)}\big) = \boldsymbol{S}\big(\boldsymbol{Q}^{(l-1)}\big) - \frac{1}{\Delta\mathcal{V}_{i,j}}\sum_{k=1}^{4} \boldsymbol{F}_k\big(\boldsymbol{Q}^{(l-1)}\big)\Delta\mathcal{S}_k \tag{15}$$

where $\boldsymbol{F}_k$ is the flux on cell side k.

The spatial discretization is performed with two matrix dissipation models: central differences augmented with a second- and fourth-order artificial viscosity of the form suggested by Turkel,[7] which we denote matrix dissipation model MDM$^{(1)}$, and a simple dissipation model, which we denote MDM$^{(2)}$.

The resulting flux with MDM$^{(1)}$ for a typical cell edge $(i+\frac{1}{2}, j)$ of a rectangular cell may be written as

$$\boldsymbol{F}_{i+\frac{1}{2},j} = \tfrac{1}{2}\Big[\boldsymbol{F}_{i,j} + \boldsymbol{F}_{i+1,j} - \boldsymbol{D}^{(2)}_{i+\frac{1}{2},j} + \boldsymbol{D}^{(4)}_{i+\frac{1}{2},j}\Big] \tag{16}$$

where the dissipation terms follow from Ref. 7 as

$$\boldsymbol{D}^{(2)}_{i+\frac{1}{2},j} = 2\big|\boldsymbol{A}_{i+\frac{1}{2},j}\big|\varepsilon^{(2)}_{i+\frac{1}{2},j}(\boldsymbol{Q}_{i+1,j} - \boldsymbol{Q}_{i,j}) \tag{17}$$

$$\boldsymbol{D}^{(4)}_{i+\frac{1}{2},j} = 2\big|\boldsymbol{A}_{i+\frac{1}{2},j}\big|\varepsilon^{(4)}_{i+\frac{1}{2},j}(\boldsymbol{Q}_{i+2,j} - 3\boldsymbol{Q}_{i+1,j} + 3\boldsymbol{Q}_{i,j} - \boldsymbol{Q}_{i-1,j}) \tag{18}$$

where $\boldsymbol{A} \equiv \partial\boldsymbol{F}/\partial\boldsymbol{Q}$ and $|\boldsymbol{A}|$ is evaluated as $\boldsymbol{T}\Lambda\boldsymbol{T}^{-1}$ with $\boldsymbol{T}$ a matrix whose columns are composed of the eigenvectors of A and Λ, a diagonal matrix whose elements are eigenvalues of $\boldsymbol{A}$, $(|u|, |u|, |u+a|, |u-a|)$. The ε terms are

$$\varepsilon^{(2)}_{i+\frac{1}{2},j} = \epsilon_2 \max(\gamma_{i,j}, \gamma_{i+1,j}) \tag{19}$$

$$\varepsilon^{(4)}_{i+\frac{1}{2},j} = \max\Big[0, \epsilon_4 - \varepsilon^{(2)}_{i+\frac{1}{2},j}\Big] \tag{20}$$

with

$$\gamma_{i,j} = \frac{|p_{i+1,j} - p_{i,j}| - |p_{i,j} - p_{i-1,j}|}{|p_{i+1,j} - p_{i,j}| + |p_{i,j} - p_{i-1,j}|} \tag{21}$$

and ϵ_2 and ϵ_4 being small positive parameters.

The second dissipation model, MDM$^{(2)}$ is similar to MDM$^{(1)}$ with the numerical flux at cell face is constructed by

$$\boldsymbol{F}_{i+\frac{1}{2},j} = \tfrac{1}{2}\big[\boldsymbol{F}(\boldsymbol{Q}^L) + \boldsymbol{F}(\boldsymbol{Q}^R)\big] - \epsilon_D(\boldsymbol{T}\Lambda\boldsymbol{T}^{-1})_{i+\frac{1}{2},j}(\boldsymbol{Q}^R - \boldsymbol{Q}^L) \tag{22}$$

with $\boldsymbol{Q}^L$ and $\boldsymbol{Q}^R$ being the values conservative variables extrapolated to the left and right sides of the interface on which the numerical flux is evaluated. The matrices $\boldsymbol{T}$ and Λ are defined following Eqs. (17) and (18). The dissipation coefficient ϵ_d is nominally set to 0.5. Further details of the implementation of this model appear in Ref. 8.

We implement the confinement through a new procedure that we term a matrix confinement procedure. We take

$$\boldsymbol{S} = \boldsymbol{S}_x + \boldsymbol{S}_y \tag{23}$$

with

$$\boldsymbol{S}_x = |\boldsymbol{A}| \begin{pmatrix} 0 \\ \epsilon_c' \rho (\hat{n} \times \boldsymbol{\omega}) \cdot \hat{i} \\ 0 \\ \epsilon_c' \rho (\hat{n} \times \boldsymbol{\omega}) \cdot u\hat{i} \end{pmatrix} \tag{24}$$

$$\boldsymbol{S}_y = |\boldsymbol{B}| \begin{pmatrix} 0 \\ 0 \\ \epsilon_c' \rho (\hat{n} \times \boldsymbol{\omega}) \cdot \hat{j} \\ \epsilon_c' \rho (\hat{n} \times \boldsymbol{\omega}) \cdot v\hat{j} \end{pmatrix} \tag{25}$$

where we have defined the flux Jacobian $\boldsymbol{A}$ earlier. The flux Jacobian $\boldsymbol{B}$ is similarly defined as $\boldsymbol{B} \equiv \partial \boldsymbol{G}/\partial \boldsymbol{Q}$.

In the present study, the dissipation parameters ϵ_2, ϵ_4, and ϵ_d and the confinement parameter ϵ_c or ϵ_c' all are free parameters, which are user specified. Generally speaking, the values of ϵ_2 and ϵ_4 are in the range of 0.01–0.5, and the typical value for ϵ_d is in the range of 0.1–0.7. Their values are selected to achieve numerical stability. A procedure for optimal selection of the confinement parameter has not yet been achieved; however, based on our experience, the value of the scalar confinement parameter ϵ_c ranges from $\mathcal{O}(0.001)$ to $\mathcal{O}(0.1)$. When matrix confinement is used, the parameter ϵ_c' is larger than the equivalent value of the scalar confinement parameter because the matrix confinement implicitly contains the grid size as a scaling factor.

Two-Dimensional Results

Supersonic Shear Layer

The first test case is an inviscid shear layer initially formed by two parallel streams, one at Mach number $M = 2.4$ and the other at $M = 2.9$. The streams are at an angle of 30 deg to a uniform 100×100 grid. The basic solver is the MDM[2] with dissipation parameter $\epsilon_d = 0.3$. Figures 1a and 1b show the computed Mach number contours for this flow. In Fig. 1a, the flow is computed with the vorticity confinement turned off. The contours represent the flow solution after 1000 time steps. The dissipation of the shear layer is evident. In Fig. 1b, we present the same computation, but with the confinement term in effect. The contours indicate practically no degradation of the shear layer. The solution presented in Fig. 1b is actually after 4000 time steps. It is essentially identical

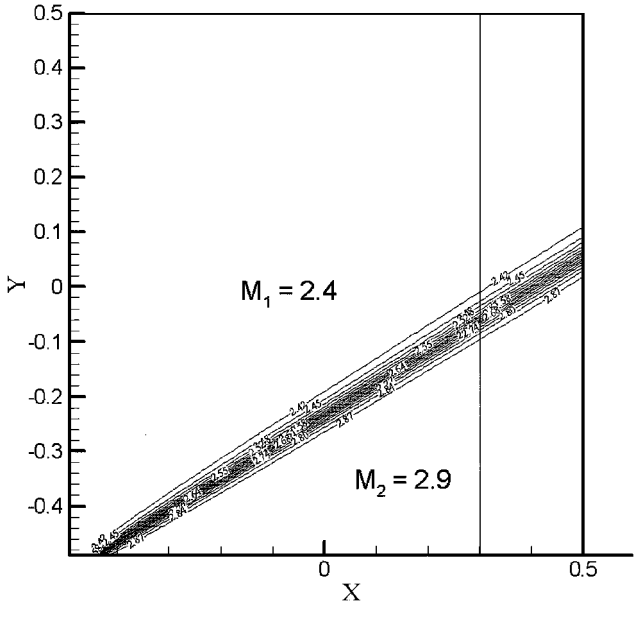

Fig. 1a Inviscid supersonic shearlayer Mach contours: no confinement, 1000 time steps.

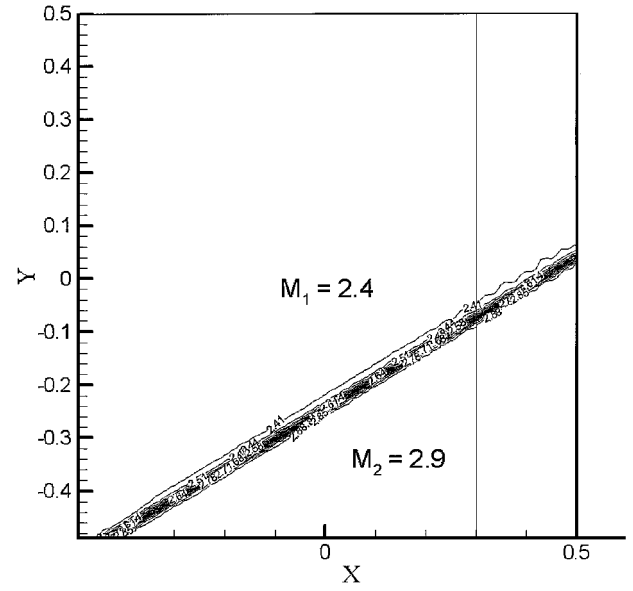

Fig. 1b Inviscid supersonic shearlayer Mach contours: with confinement, 4000 time steps.

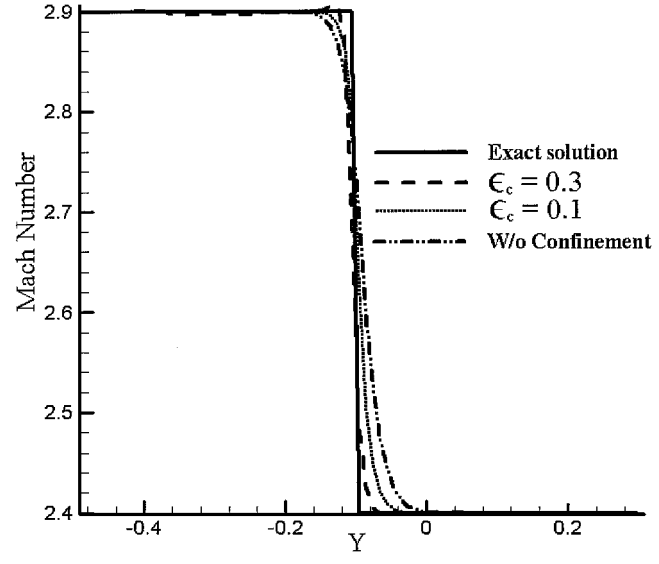

Fig. 2 Mach number distribution along a vertical cut in a supersonic shear layer.

to the solution after 1000 steps. Without confinement, the solution presented in Fig. 1a would have significantly degraded with additional computation. This is quantified in Fig. 2, which presents the Mach number along a vertical cut marked in Figs. 1a and 1b.

The classical accuracy of the solution for this problem has been investigated by performing the calculation on three sets of grids, 200×200, 100×100, and 50×50 for ϵ_c varying from 0 to 0.3. Figure 3 presents the L_2 norm of the error between the computed Mach number distribution and the exact (nondissipated) Mach number distribution. With the analysis of Fig. 3 we have two findings: 1) The error decreases as the grid size decreases when confinement parameter is fixed at an appropriate value. 2) The error decreases as the confinement parameter increases within an appropriate range when the grid size is fixed. Therefore, the effect of decreasing the grid size (increasing the number of grid points) is similar to increasing confinement parameter within an appropriate range when the grid size is fixed. Furthermore, the conclusion just drawn can be reached by accuracy analysis presented in Fig. 4, which shows the slope of the log of the norm of the error with respect to the $\log(\Delta x)$. From Fig. 4, we see an improvement in the error with increasing value of confinement parameter, with $\epsilon_c = 0.3$ achieving close to second-order accuracy.

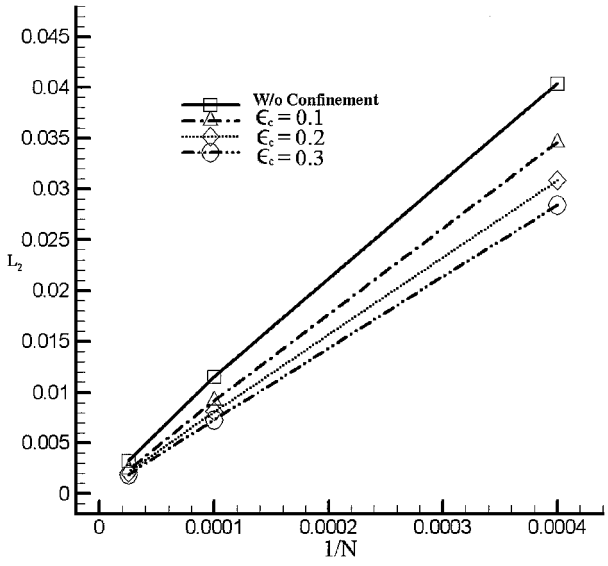

Fig. 3 Error norm vs grid size for supersonic shear flow calculations.

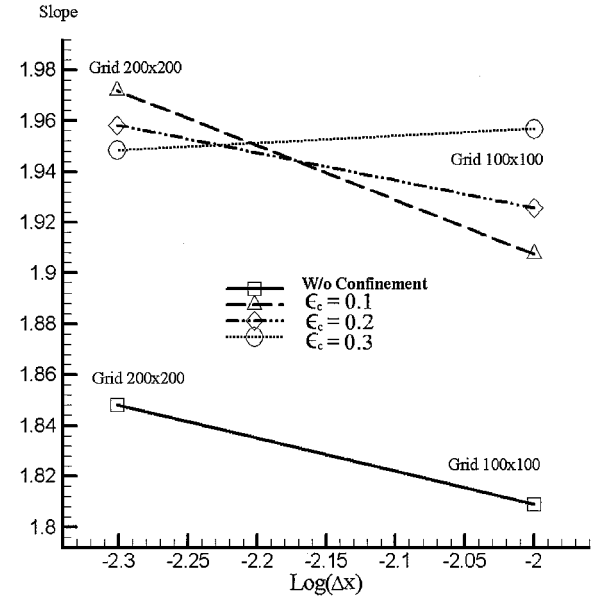

Fig. 4 Slope of the log of the error norm with respect to log(Δx).

Vortex Moving in a Uniform Flow

The second test case is a vortex moving in a freestream. We model the initial conditions of the vortex in a simplified manner as suggested in Ref. 9. We prescribe an inviscid vortical velocity distribution between an outer radius $r = R_o$ and a core radius $r = R_c$. Outside R_o the tangential velocity is set to zero. Inside the core $r < R_c$, the velocity goes linearly to zero at $r = 0$. This results in the following tangential velocity profile:

$$u_\theta(r) = \begin{cases} U_c r/R_c, & r < R_c \\ Ar + B/r, & R_c \le r \le R_o \end{cases} \tag{26}$$

where

$$A = -\frac{U_c R_c}{R_o^2 - R_c^2}, \qquad B = \frac{U_c R_o^2 R_c}{R_o^2 - R_c^2} \tag{27}$$

and which results in $u_\theta(0) = 0$, $u_\theta(R_c) = U_c$, and $u_\theta(R_o) = 0$. The velocity U_c at $r = R_c$ is a parameter. This initial vortex is added to a uniform stream $\boldsymbol{V} = U_\infty \hat{i}$. We perform the calculation with $R_c = 0.05$ m, $R_o = 10R_c$, $a_\infty = 347.2$ m/s, $U_\infty = a_\infty/2$, and $U_c = U_\infty$. The calculation was carried out using MDM[1] with dissipation parameters $\epsilon_2 = 0.01$, $\epsilon_4 = 0.30$, and the confinement

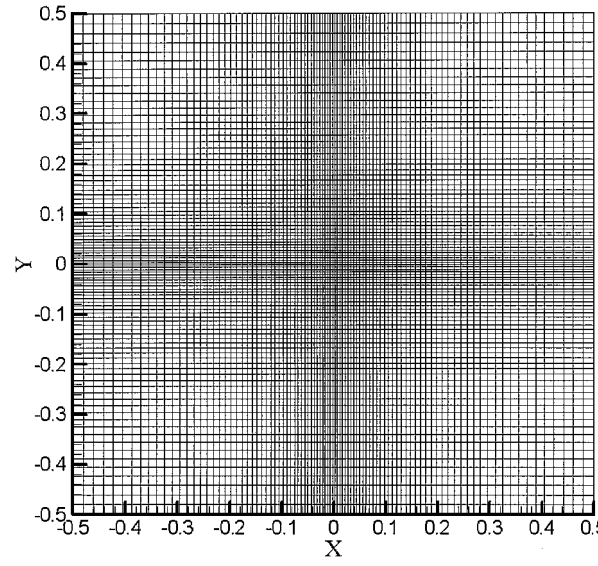

Fig. 5 Nonuniform grid distribution for calculations of a vortex moving with a freestream.

parameter $\epsilon_c = 0.60$. We perform the calculations on a 100×100 grid. The grid is stretched and spatially varying in both directions. A non-uniform grid is used to test the efficiency of the confinement scheme. The axial grid is distributed according to an exponential function:

$$x_i = x_1 + [(e^{k\beta} - 1)/(e^\beta - 1)](x_{i_{\max}} - x_1) \tag{28}$$

with $k = (i-1)/(i_{\max} - 1)$ and $i = 1, \ldots, i_{\max}$. We set the parameters $\beta = 1.5$, $x_1 = 0.0022$, $x_{i_{\max}} = 0.5$, and $i_{\max} = 50$, which results in a minimum grid spacing of $\Delta x = 0.0044$ located at the center of the domain. The grid is symmetric about the x and y coordinates. A grid of 100×100 is presented in Fig. 5. The computational boundary is a square 1×1 m. We apply periodic boundary conditions on all edges of the domain. The computed vortex will then pass through the grid and reappear on the other side.

The analytic solution for a compressible vortex moving with a uniform freestream is discussed in Ref. 8. The solution contains the well-known result that the quantity ω/ρ of a vortex will be conserved as it convects in a compressible, inviscid, adiabatic fluid. First, we present the computation without vorticity confinement. In Fig. 6a, we present the contours of the quantity ω/ρ of the flow solution after the vortex has passed through the grid roughly one time and is approximately centered in the computational domain. Figure 6b presents the same calculation, but after passing through the grid 10 times. The degree of dissipation is quite evident. Next, in Figs. 7a and 7b, we present the identical calculations, but with the vorticity confinement turned on. Figures 7a and 7b indicate no apparent degradation of the vorticity contours. The profile of the quantity ω/ρ along a cut through the diameter of the moving vortex is presented in Fig. 8a. From Fig. 8a, we see that the solutions without confinement have been greatly affected by the numerical dissipation, with eventually all ω/ρ damped out. On the other hand, the solutions with confinement do not show this dissipative behavior even though the vortex passed the grid 10 times. The vorticity confinement terms effectively balance the numerical dissipation and produce results where the vorticity distribution remains unchanged with time. The confinement solution is in good agreement with the analytical solution except for some wiggles developed near $r = R_c$, which may be caused by the interaction of the freestream and the edge of the core of the vortex where there exists strong velocity and vorticity gradients.

The results indicate that the method is successful in confining the vorticity for a case where the vortex is adequately resolved by the grid. However, in many CFD applications, we do not currently have this luxury. In Fig. 8b, we present a calculation where we dramatically reduced the grid to 12×12. For this calculation we use the same dissipation parameters $\epsilon_2 = 0.01$ and $\epsilon_4 = 0.30$ and

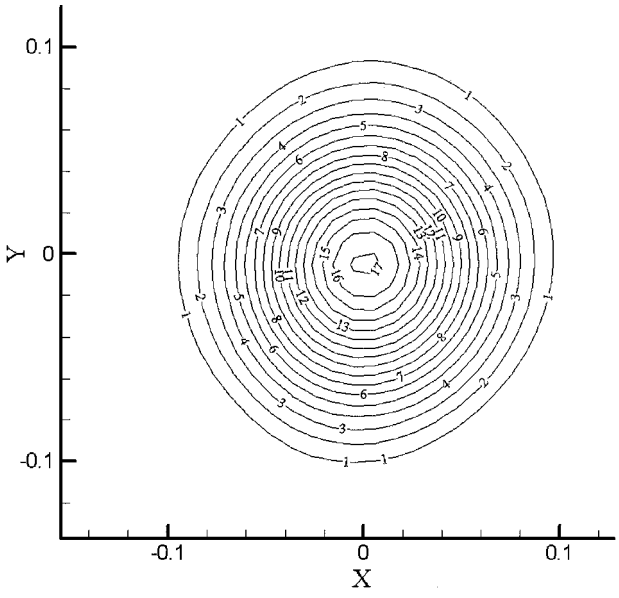

Fig. 6a Contours of vorticity over density after one circuit for a vortex moving with a freestream: no vorticity confinement.

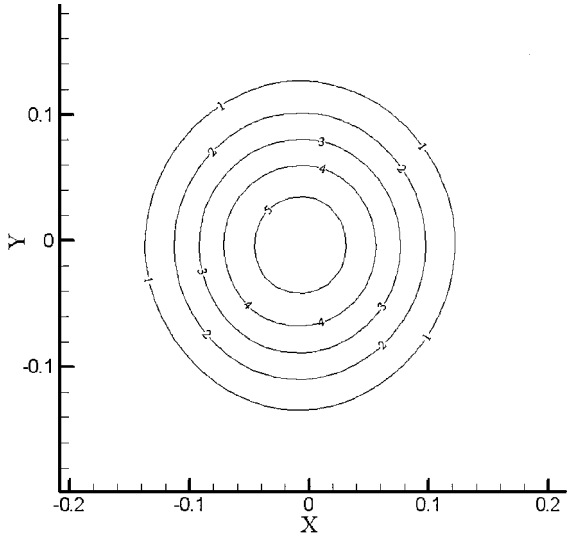

Fig. 6b Contours of vorticity over density after 10 circuits for a vortex moving with a freestream: no vorticity confinement.

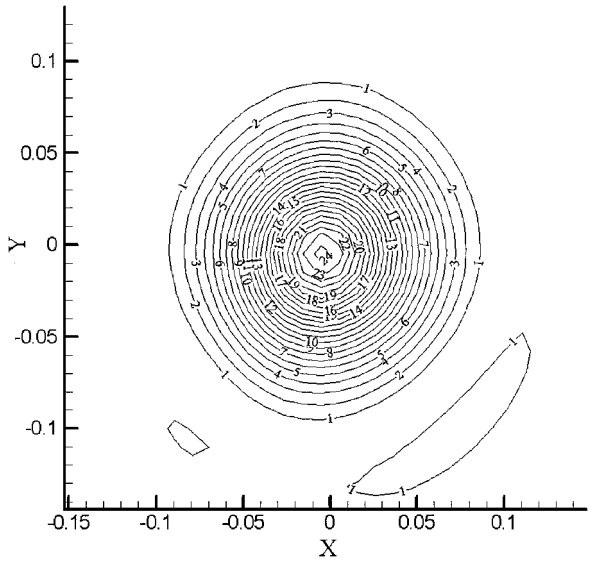

Fig. 7a Contours of vorticity over density after one circuit for a vortex moving with a freestream: solution with vorticity confinement.

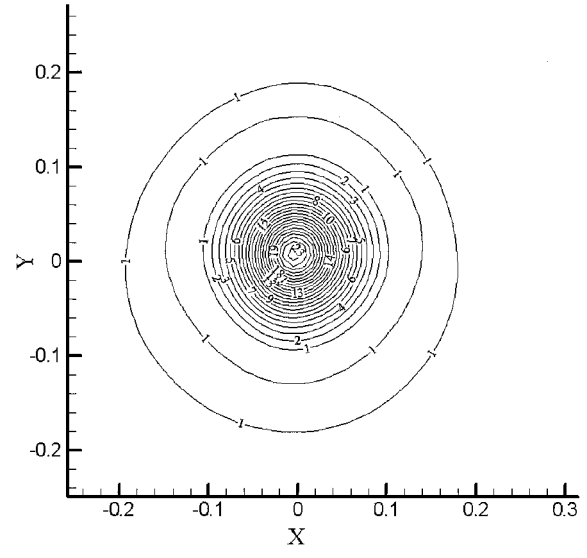

Fig. 7b Contours of vorticity over density after 10 circuits for a vortex moving with a freestream: solution with vorticity confinement.

increase the confinement parameter $\epsilon_c = 1.33$. The profile of the quantity ω/ρ along a vertical slice taken through the center of the vortex after 1, 10, or 20 circuits indicates very little dissipation, even for this case with only four–six cells across the vortex. There is certainly a degradation in the value of ω/ρ near the core, but it essentially does not further degrade with time.

Supersonic Conical Flow Results

To illustrate the capability of the compressible vorticity confinement procedure, we consider the application to supersonic conical flows. These flowfields, although depending only on two coordinate values, exhibit many important three-dimensional effects for the supersonic flow past wings and bodies. Inviscid supersonic flows over arbitrary conical bodies with attached bow shocks fall into this category. We begin with a transformation to a conical coordinate system (r, ξ, η) that is related to Cartesian coordinates as

$$r = \sqrt{x^2 + y^2 + z^2}, \qquad \xi = y/x, \qquad \eta = z/x \tag{29}$$

where the axis of the body is along the x coordinate direction. In this system, all flow quantities will be independent of the spherical radius r such that the governing Euler equations (cf., Powell[10]) may be written as

$$\frac{r}{k}\frac{\partial \boldsymbol{Q}}{\partial t} + \frac{\partial \tilde{\boldsymbol{G}}}{\partial \xi} + \frac{\partial \tilde{\boldsymbol{H}}}{\partial \eta} + 2\boldsymbol{F} = -\frac{r}{k}\boldsymbol{S} \tag{30}$$

where $k = \sqrt{(1 + \xi^2 + \eta^2)}$ and

$$\boldsymbol{Q} = \begin{pmatrix} \rho \\ \rho u \\ \rho v \\ \rho w \\ \rho e_0 \end{pmatrix}, \qquad \boldsymbol{F} = \begin{pmatrix} \rho u \\ \rho u^2 + p \\ \rho uv \\ \rho uw \\ \rho u h_0 \end{pmatrix}$$

$$\tilde{\boldsymbol{G}} = \begin{pmatrix} \rho \tilde{v} \\ \rho u \tilde{v} - \xi p \\ \rho v \tilde{v} + p \\ \rho w \tilde{v} \\ \rho \tilde{v} h_0 \end{pmatrix}, \qquad \tilde{\boldsymbol{H}} = \begin{pmatrix} \rho \tilde{w} \\ \rho u \tilde{w} - \eta p \\ \rho v \tilde{w} \\ \rho w \tilde{w} + p \\ \rho \tilde{w} h_0 \end{pmatrix} \tag{31}$$

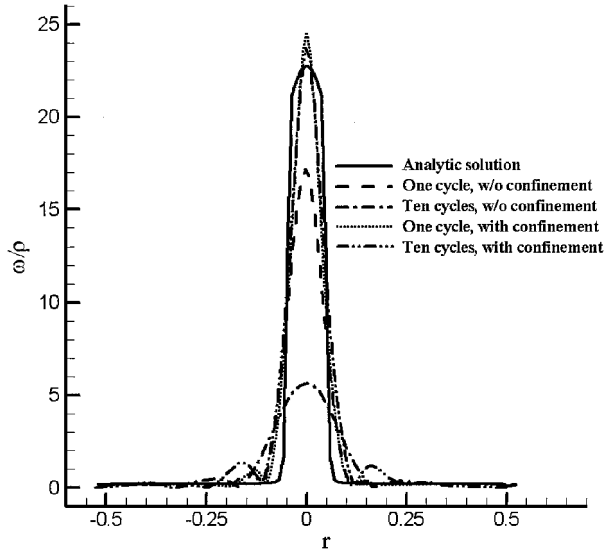

Fig. 8a Vorticity/density ratio distribution along a slice through a vortex moving with a freestream. Comparison between confined and unconfined results on a relatively fine 100 × 100 grid.

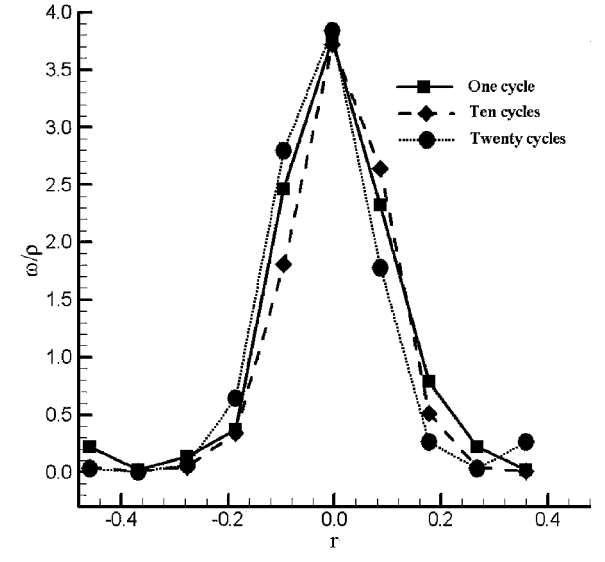

Fig. 8b Vorticity/density ratio distribution along a slice through a vortex moving with a freestream. Confined results on a very coarse 12 × 12 grid presented after 1, 10, and 20 circuits of the grid.

The covariant velocity components may be written as

$$\tilde{u} = u + \xi v + \eta w, \qquad \tilde{v} = v - \xi u, \qquad \tilde{w} = w - \eta u \tag{32}$$

and the matrix confinement term as

$$\boldsymbol{S} = \boldsymbol{S}_x + \boldsymbol{S}_y + \boldsymbol{S}_z \tag{33}$$

For conical flows, we base the confinement term, Eq. (8), on the crossflow vorticity, $\omega_r = \boldsymbol{\omega} \cdot \hat{i}_r$. Thus, we take

$$\boldsymbol{f}_b = -\epsilon_c \hat{n} \times (\omega_r \hat{i}_r) \tag{34}$$

with

$$\hat{n} = -\nabla(\omega_r)/|\nabla(\omega_r)| \tag{35}$$

Using the definition of vorticity and the coordinate transformation in Eqs. (29), we can develop an expression for the crossflow vorticity in terms of Cartesian velocity components as

$$\omega_r = \frac{1}{r}\left[\frac{\partial w}{\partial \xi} - \frac{\partial v}{\partial \eta} + \xi\left(\frac{\partial u}{\partial \eta} + \xi\frac{\partial w}{\partial \xi} + \eta\frac{\partial w}{\partial \eta}\right) - \eta\left(\frac{\partial u}{\partial \xi} + \xi\frac{\partial v}{\partial \xi} + \eta\frac{\partial v}{\partial \eta}\right)\right] \tag{36}$$

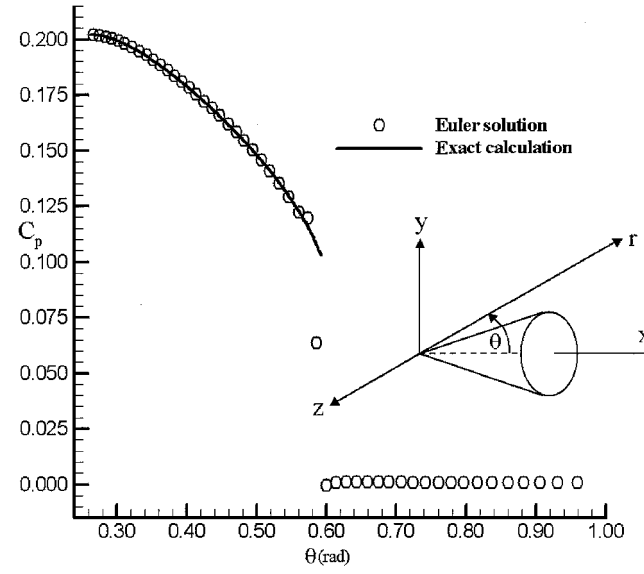

Fig. 9 Pressure distribution in the shock layer of a circular cone at zero incidence, $M_\infty = 2$ and $\theta_c = 15$ deg.

Computations are performed on a grid generated in the ξ–η plane using a modified Joukowski transformation from the complex ζ plane as

$$\xi + i\eta = \zeta + (c^2/\zeta) \tag{37}$$

where

$$c^2 = \tfrac{1}{4}[\tan^2(\pi/2 - \beta) - \tan^2\delta] \tag{38}$$

with β the half-angle of the major axis of the elliptic cone (leading-edge angle) and δ the half-angle of the minor axis of the elliptic cone. The radius of the circle in the ζ plane corresponding to the surface of the elliptic cone is

$$|\zeta_b| = \tfrac{1}{2}[\tan(\pi/2 - \beta) + \tan\delta] \tag{39}$$

First, we present a computation of a 15-deg half-angle circular cone at zero incidence to establish the accuracy level of the basic code. The calculation is done without confinement using an explicit four-stage Runge–Kutta time-stepping procedure and dissipation parameters $\epsilon_2 = 0.15$ and $\epsilon_4 = 0.01$. The calculation was performed on a grid with 64 mesh points in the circumferential direction (half-cone) and 51 mesh points in the azimuthal direction. The pressure coefficient distribution in the shock layer is presented in Fig. 9. The agreement with the accurate Taylor–Maccoll solution (see Ref. 11) is excellent. The bow shock is accurately captured within two mesh intervals.

Next we present two calculations for a flat plate delta wing at high incidence. These cases illustrate the ability of the method to capture vortices from sharp leading edges of wings accurately. The first case corresponds to a Mach number $M_\infty = 1.7$, angle of attack $\alpha = 12$ deg, and a sweep-back angle of $\Lambda = 75$ deg. The calculations were performed on a 64 × 64 uniform grid in the mapped plane with dissipation parameters set to $\epsilon_2 = 0.1$ and $\epsilon_4 = 0.005$ and the matrix confinement parameter set to $\epsilon_c' = 15.0$. The details of the flowfield solution are shown in Figs. 10a–10d. The pressure contours and the Mach number contours in Figs. 10a and 10b, respectively, show the low-pressure region on the leeward surface and the crossflow shock. The crossflow velocity vectors and crossflow streamlines in Figs. 10c and 10d, respectively, indicate the size and strength of the vortex.

In Fig. 11, we present the distribution of the pressure coefficient on the surface of the wing. Shown in Fig. 11 are the solutions calculated both with confinement and without confinement. We also present the experimental data of Miller and Wood[12] as discussed in Ref. 10. The confined solution is in good agreement with the data, including the crossflow shock. Also, plotted in Fig. 11 is the Euler solution of Powell[10] performed on an equivalent 128 × 128 grid with local grid refinement in the vicinity of the vortex and the leading edge. Even

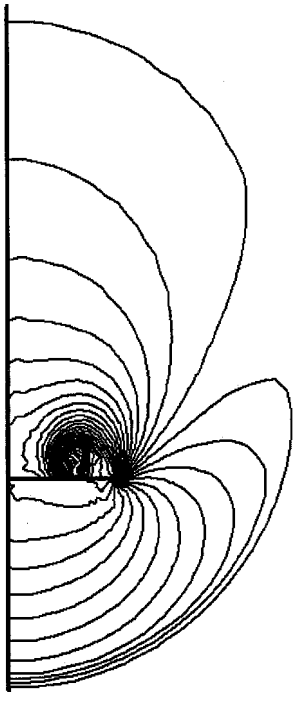

Fig. 10a Pressure contours on a flat delta wing at $\alpha = 12$ deg, $M_\infty = 1.7$, and $\Lambda = 75$ deg: 40 contour levels, $-0.42 \leq C_p \leq 0.19$.

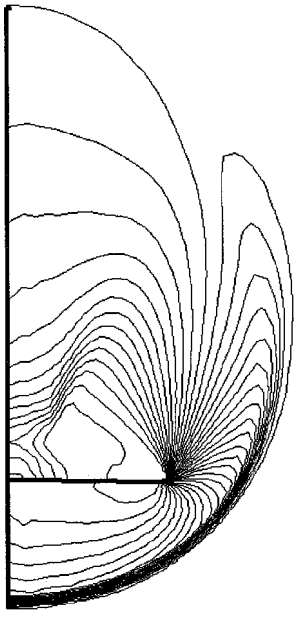

Fig. 10b Mach number contours on a flat delta wing at $\alpha = 12$ deg, $M_\infty = 1.7$, and $\Lambda = 75$ deg: 40 contour levels, $1.47 \leq M \leq 2.64$.

though the confined solution is not locally refined and is performed on a coarser grid, we obtained nearly the same suction peak, the same position, and the same size of the primary vortex as measured in the experiment. Reference 10 overpredicted the suction peak and predicted the primary vortex that was larger and more outboard than the measured one. We observe that in this complex, supersonic vortex-dominated flow, the pressure coefficient not only depends on the primary vortex but also depends on the crossflow shocks and their interaction. Vorticity confinement appears to play an important role in obtaining good agreement with experiment.

Next, we present another case of a flat plate delta wing at higher incidence. This case corresponds to a higher Mach number of $M_\infty = 2.8$, higher angle of attack of $\alpha = 20$ deg, and the same sweep-back angle of $\Lambda = 75$ deg. The calculations were performed on the same 64×64 grid in the mapped plane with dissipation parameters set to $\epsilon_2 = 0.2$ and $\epsilon_4 = 0.01$ and the matrix confinement parameter set to $\epsilon_c' = 15.0$. The details of the flowfield solution are shown in Figs. 12a–12d. The pressure contours and the Mach number contours in Figs. 12a and 12b, respectively, show a complex low-pressure region on the leeward surface and indicate a strong windward bow shock. In the Mach number contours is evidence

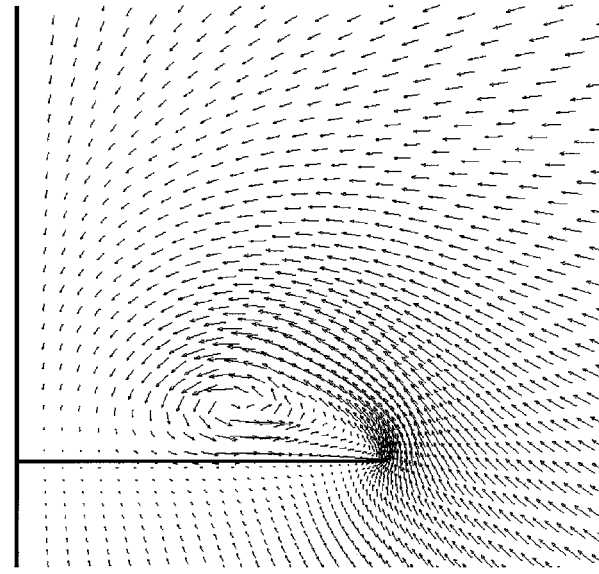

Fig. 10c Crossflow velocity vectors on a flat delta wing at $\alpha = 12$ deg, $M_\infty = 1.7$, and $\Lambda = 75$ deg.

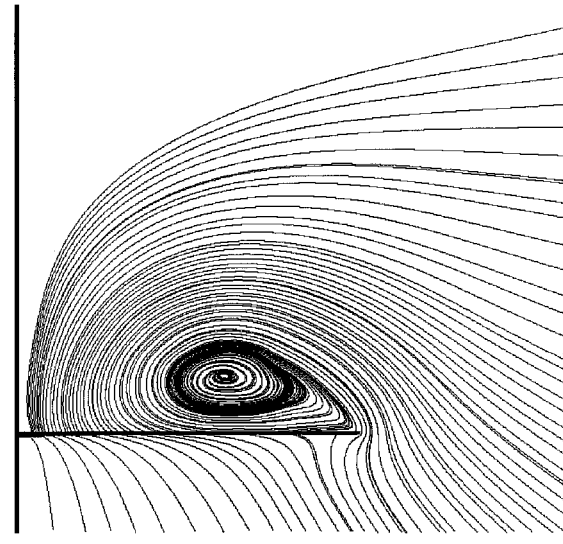

Fig. 10d Crossflow streamlines on a flat delta wing at $\alpha = 12$ deg, $M_\infty = 1.7$, and $\Lambda = 75$ deg.

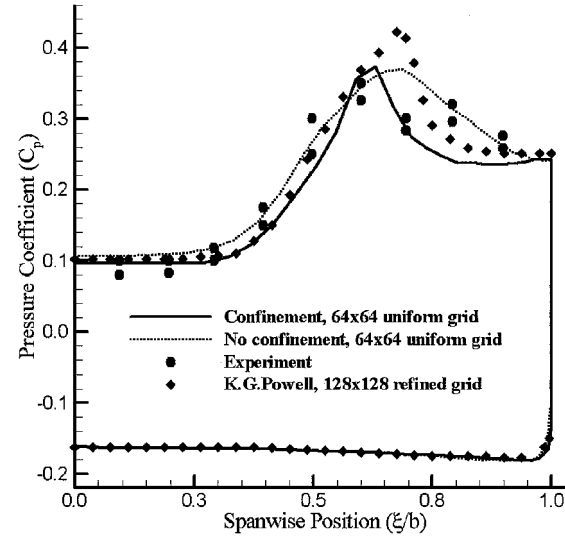

Fig. 11 Surface pressure distribution on a flat delta wing at $\alpha = 12$ deg, $M_\infty = 1.7$, and $\Lambda = 75$ deg: comparison with experimental data and unconfined refined grid calculation.[10]

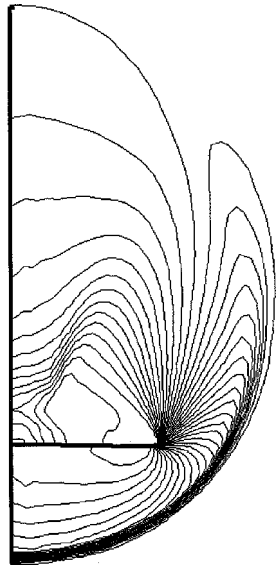

Fig. 12a Pressure contours on a flat delta wing at $\alpha = 20$ deg, $M_\infty = 2.8$, and $\Lambda = 75$ deg: 40 contour levels, $-0.18 \leq C_p \leq 0.32$.

Fig. 12b Mach number contours on a flat delta wing at $\alpha = 20$ deg, $M_\infty = 2.8$, and $\Lambda = 75$ deg: 40 contour levels, $2.1 \leq M \leq 4.9$.

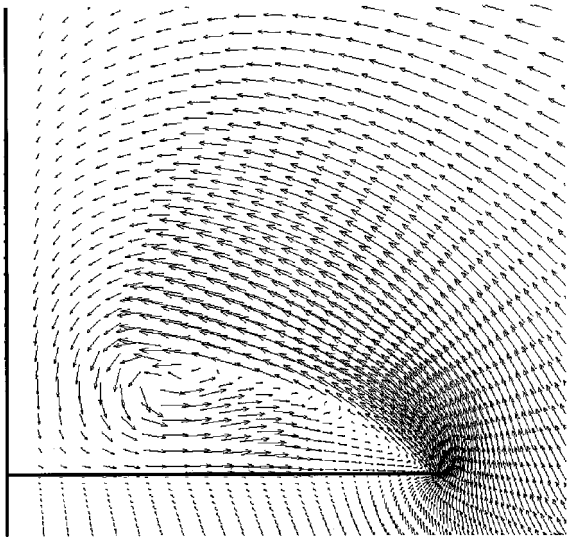

Fig. 12c Crossflow velocity vectors on a flat delta wing at $\alpha = 20$ deg, $M_\infty = 2.8$, and $\Lambda = 75$ deg.

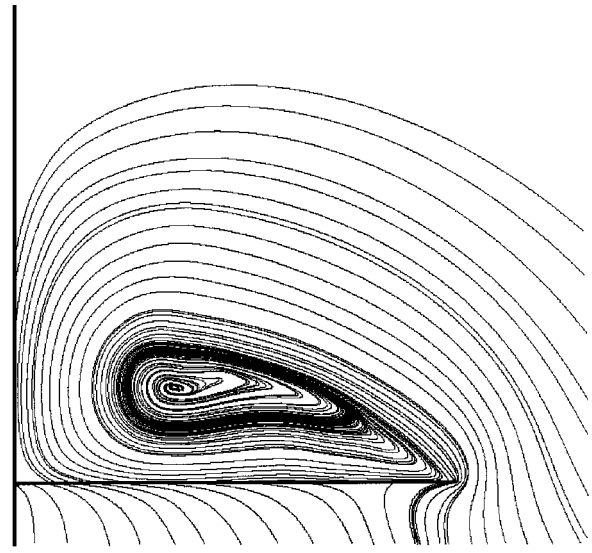

Fig. 12d Crossflow streamlines on a flat delta wing at $\alpha = 20$ deg, $M_\infty = 2.8$, and $\Lambda = 75$ deg.

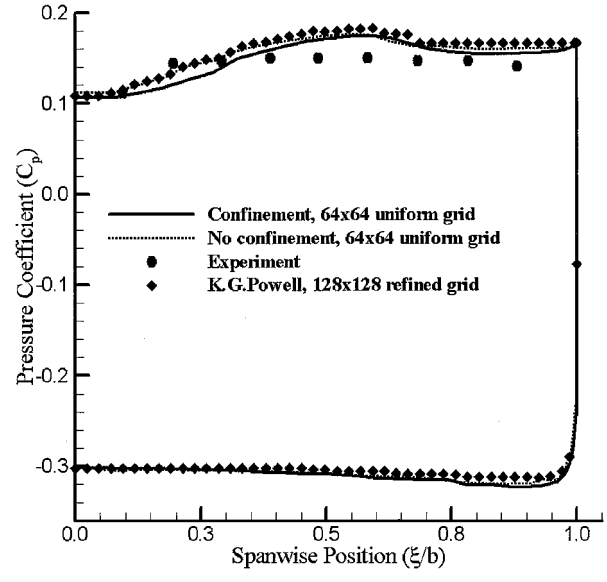

Fig. 13 Surface pressure distribution on a flat delta wing at $\alpha = 20$ deg, $M_\infty = 2.8$, and $\Lambda = 75$ deg: comparison with experimental data and unconfined refined grid calculation.[10]

of a crossflow shock underneath the vortex. The crossflow velocity vectors and crossflow streamlines in Figs. 12c and 12d, respectively, indicate the large region of separated flow.

In Fig. 13, we present the distribution of the pressure coefficient on the surface of the wing. Shown on the plot are the solutions calculated both with confinement and without confinement. We also present the experimental data of Miller and Wood[12] as discussed in Ref. 10. Also shown in the plot is the Euler solution of Powell[10] performed on an equivalent 128×128 grid with local grid refinement in the vicinity of the vortex and the leading edge. For this case, even though the flowfield on the leeward surface is quite complex, the pressure distribution is relatively flat.

Conclusions

In this paper we have successfully extended Steinhoff's vorticity confinement procedure[1,2] to compressible flows. The extension was based on basic principles and resulted in a modification of the compressible conservation laws to allow for the introduction of vorticity confinement consistently. A finite volume procedure was then developed that incorporated a matrix artificial dissipation and a new matrix confinement term. Preliminary results on supersonic shear layers and for moving vortices showed that the confinement term

allows the capture of vortical layers that effectively do not decay in time, even on coarse grids. Calculations of the vortex separation on the leeward surface of a flat plate delta wing at supersonic speed indicate good agreement with data and show the potential of the method for handling complex three-dimensional flowfields, particularly those with thin vortical regions.

The methodology must still be proven on geometrically complex three-dimensional flowfields involving highly skewed grids. If a suitable scaling could be found, the method might be useful as an add-on to existing CFD codes.

References

[1]Steinhoff, J., Wang, C., Underhill, D., Mersch, T., and Wenren, Y., "Computational Vorticity Confinement: A Non-Diffussive Eulerian Method for Vortex-Dominated Flows," Univ. of Tennessee Space Inst., Preprint, Tullahoma, TN, 1992.

[2]Steinhoff, J., "Vorticity Confinement: A New Technique for Computing Vortex Dominated Flows," *Frontiers of Computational Fluid Dynamics*, edited by D. A. Caughy and M. M. Hafez, Wiley, New York, 1994, pp. 235–263.

[3]Steinhoff, J., Puskas, E., Babu, S., Wenren, Y., and Underhill, D., "Computation of Thin Features over Long Distances Using Solitary Waves," *Proceedings of the AIAA 13th Computational Fluid Dynamics Conference*, AIAA, Reston, VA, 1997, pp. 743–759.

[4]Steinhoff, J., Wenren, Y., and Wang, L., "Efficient Computation of Separating High Reynolds Number Incompressible Flows Using Vorticity Confinement," AIAA Paper 99-3316, June 1999.

[5]Pevchin, S., Grossman, B., and Steinhoff, J., "Capture of Contact Discontinuities and Shock Waves Using a Discontinuity Confinement Procedure," AIAA Paper 97-0874, Jan. 1997.

[6]Yee, K., and Lee, D.-H., "Euler Calculation for a Hovering Coaxial Rotor Flow Field with New Boundary Condition," *Proceedings of the 24th European Rotorcraft Forum*, Marseilles, France, 1998, pp. AE-1–AE-10.

[7]Turkel, E., "Improving the Accuracy of Central Difference Schemes," *Lecture Notes in Physics*, Vol. 323, Springer, 1988, pp. 586–591.

[8]Hu, G., "The Development and Applications of a Numerical Method for Compressible Vorticity Confinement in Vortex-Dominant Flows," Ph.D. Dissertation, Dept. of Aerospace and Ocean Engineering, Virginia Polytechnic Inst. and State Univ., Blacksburg, VA, June 2001; also URL: http://scholar.lib.vt.edu/theses/available/etd-08042001-122806/.

[9]Povitsky, A., and Ofengeim, D., "Numerical Study of Interaction of a Vortical Density Inhomogeneity with Shock and Expansion Waves," ICASE, Rept. 98-10, Hampton, VA, Feb. 1998.

[10]Powell, K. G., *Vortical Solutions of the Conical Euler Equations*, Vol. 28, Notes on Numerical Fluid Mechanics, Vieweg, Braunschweig, Germany, 1990, pp. 121–127, 138–145.

[11]Anderson, J. D., Jr., *Modern Compressible Flow with Historical Perspective*, 2nd ed., McGraw–Hill, New York, 1990, pp. 296–306.

[12]Miller, D. S., and Wood, R. M., "Lee-Side Flow over Delta Wings at Supersonic Speeds," NASA TP 2430, June 1985.

P. Givi
Associate Editor